Chalcogenide Letters Vol. 22, No. 10, October 2025, p. 889 - 904

Adsorption behavior and mechanism of heavy metal ions from acid mine drainage using two-dimensional MoS_2 nanosheets

K. Wang [a,b,*], G. L. Lian [c], Y. F. Qiao [d]

[a] *Engineering Training Center, Shanxi Institute of Technology, Yangquan, 045000, China*

[b] *School of Mines, China University of Mining and Technology, Xuzhou, 221116, China*

[c] *Zhongmei Huajin Group Jincheng Energy Co., Ltd. Jincheng, 048000, China*

[d] *Department of Electrical and Control Engineering, Shanxi Institute of Technology, Yangquan, 045000, China*

The remediation of acid mine drainage (AMD), characterized by its high concentrations of toxic metal ions and low pH, presents a significant environmental challenge. In this study, exfoliated two-dimensional MoS_2 nanosheets were prepared using a liquid-phase ultrasonication method and evaluated for their efficiency in removing Cd^{2+}, Cu^{2+}, and Pb^{2+} from aqueous solutions. Detailed structural and morphological analyses confirmed that the exfoliation process significantly enhanced surface area, pore volume, and exposure of reactive sulfur sites. Through isotherm and kinetic modeling analyses, the adsorption behavior was found to align with the Langmuir model and pseudo-second-order kinetic equation, which implies that monolayer chemisorption serves as the primary adsorption mechanism. Spectroscopic characterizations revealed the formation of stable metal–sulfur complexes, highlighting the pivotal role of sulfur functional groups in binding metal ions. The developed MoS_2 nanosheets demonstrated rapid adsorption kinetics and high removal efficiencies under optimal conditions, confirming their potential as a highly effective and sustainable material for heavy metal remediation in complex aqueous environments.

(Received May 21, 2025; Accepted October 10, 2025)

Keywords: Surface functionalization, Adsorption kinetics, Environmental remediation, Spectroscopic analysis, Nanostructured materials

1. Introduction

The relentless expansion of mining and industrial activities has inadvertently introduced severe environmental challenges, among which acid mine drainage (AMD) stands as a particularly critical issue [1]. AMD is characterized by its low pH [2] and high concentrations of dissolved heavy metal ions [3]. These toxic elements, once released into natural water bodies, pose significant threats to aquatic ecosystems and human health [4]. Owing to their non-biodegradable characteristic, heavy metals tend to build up within living organisms, giving rise to bioaccumulation and facilitating

* Corresponding author: LB18020007@cumt.edu.cn

https://doi.org/10.15251/CL.2025.2210.889

biomagnification along food chains [5]. The alarming persistence and toxicity of these contaminants necessitate the development of effective and sustainable remediation strategies capable of removing heavy metal ions from AMD before their uncontrolled dispersion into the environment.

Traditional methods for treating AMD, including chemical precipitation, ion exchange, membrane filtration, and biological treatments, have been widely investigated and applied [6]. However, these approaches often suffer from several limitations, including high operational costs, sludge generation, complex operational requirements, and limited removal efficiency under low metal ion concentrations [7]. Adsorption has emerged as one of the most promising alternatives [8]. Among different types of adsorbents, materials like activated carbon, zeolites, and clay minerals have been widely applied [9]. Despite their widespread application, these materials exhibit relatively low adsorption capacities for heavy metals, limited regeneration potential, and poor selectivity, which significantly restrict their practical usage in large-scale AMD treatment.

In recent years, the advent of nanomaterials has introduced new possibilities for addressing the challenges of heavy metal remediation [10]. Owing to their unique physicochemical properties, including high surface area-to-volume ratio, tunable surface chemistry, and abundant active sites, nanomaterials offer significantly improved adsorption capacities [11] and faster reaction kinetics compared to their bulk counterparts. Among these advanced materials, 2D nanostructures have attracted substantial interest due to their exceptional surface reactivity and distinctive layered architectures [12]. These materials provide a wealth of accessible adsorption sites and exhibit unique electronic, optical, and catalytic properties [13] that are highly desirable for environmental applications.

Within the family of 2D nanomaterials, molybdenum disulfide (MoS_2) has gained particular attention as a highly promising adsorbent for the removal of heavy metal ions from contaminated waters. This structure facilitates easy exfoliation into ultrathin nanosheets, dramatically increasing the material's accessible surface area [14]. More importantly, the exposed sulfur atoms on the edges and basal planes of MoS_2 nanosheets play a pivotal role in metal ion adsorption through strong chemical interactions, such as coordination and complexation, particularly with soft heavy metal ions like Cd^{2+}, Pb^{2+}, and Cu^{2+}. The high affinity of sulfur toward heavy metal ions makes MoS_2 an ideal candidate for selective adsorption applications. While bulk MoS_2 has been explored for environmental remediation, its application has been hindered by limited surface area, poor accessibility of active sites, and sluggish adsorption kinetics. The tightly stacked layers in bulk MoS_2 restrict the diffusion of metal ions to the active adsorption sites, leading to suboptimal performance. In contrast, exfoliated two-dimensional MoS_2 nanosheets offer significant improvements in adsorption efficiency due to their expanded interlayer spacing, higher defect densities, and greater exposure of reactive sulfur sites.

Despite the promising properties of MoS_2 nanosheets, several knowledge gaps remain [15]. Existing studies have primarily focused on the synthesis of MoS_2 nanosheets and their general adsorption performance, often under idealized laboratory conditions [16]. Comparative evaluations of bulk versus nanosheet MoS_2 under identical experimental conditions remain scarce, leaving unanswered questions about the true extent of performance enhancement achieved through exfoliation. Moreover, the underlying mechanisms governing the adsorption of heavy metal ions onto MoS_2 nanosheets require further elucidation [17]. Detailed understanding of the roles played by physical adsorption, electrostatic interactions, and chemical complexation is essential to optimize material design and tailor adsorption conditions for maximum efficiency.

To bridge these gaps, it is crucial to undertake a systematic investigation that combines comprehensive material characterization with rigorous adsorption performance assessments. Coupling these analyses with adsorption isotherm and kinetic modeling can unravel the complex interplay of adsorption mechanisms, offering a more complete picture of the heavy metal removal process. This study aims to address these research gaps by synthesizing and characterizing two-dimensional MoS_2 nanosheets using a scalable liquid-phase exfoliation technique and comparing their adsorption performance with bulk MoS_2 for the removal of heavy metal ions from acid mine drainage. Emphasis is placed on understanding how structural modifications—specifically, increased surface area, expanded interlayer spacing, and exposure of reactive sulfur sites—affect the adsorption behavior and efficiency of MoS_2. Additionally, the adsorption mechanisms are investigated through the analysis of isotherm models, kinetic studies, and post-adsorption material characterization, providing valuable insights into the design of more effective adsorbents for AMD remediation.

2. Materials and methods

2.1. Materials

All reagents used in this study were of analytical grade and employed without further purification. Bulk molybdenum disulfide (MoS_2) powder was procured from Aladdin Reagent Co., Ltd. (Shanghai, China). Ammonium tetrathiomolybdate ($(NH_4)_2MoS_4$, 99%) and hydrazine hydrate ($N_2H_4 \cdot H_2O$, 80%) were purchased from Sinopharm Chemical Reagent Co., Ltd. All metal salts for adsorption studies, including ($Cd(NO_3)_2 \cdot 4H_2O$), ($CuSO_4 \cdot 5H_2O$), and ($Pb(NO_3)_2$), were obtained from Tianjin Damao Chemical Reagent Factory (Tianjin, China).

2.2. Synthesis of MoS_2 nanosheets

MoS_2 nanosheets were synthesized using a liquid-phase exfoliation technique facilitated by ultrasonication and a quenching-assisted dispersion process. Initially, 5 g of bulk MoS_2 powder was dispersed in 250 mL of a 1:1 volume ratio mixture of isopropanol and water. The suspension was stirred vigorously for 1 hour to ensure uniform dispersion [18]. Following this, the mixture was subjected to ultrasonication using a high-power probe sonicator (JY92-IIDN, Ningbo Scientz Biotechnology Co., Ltd., China) operated at 500 W and a frequency of 20 kHz. The sonication was conducted under an ice-water bath to prevent overheating, and the process lasted for 8 hours with intermittent pulses of 5 seconds on and 2 seconds off to maintain dispersion efficiency.

After sonication, the resulting suspension was immediately subjected to a rapid freezing process by immersing it in liquid nitrogen for 30 minutes, followed by thawing at room temperature. This quenching process was repeated three times to promote further exfoliation and prevent restacking of nanosheets. Subsequently, the suspension was centrifuged at 3000 rpm for 30 minutes using a high-speed centrifuge to remove unexfoliated bulk materials. The supernatant containing the exfoliated MoS_2 nanosheets was collected and further purified by repeated washing with deionized water through centrifugation at 8000 rpm for 20 minutes to remove residual solvents. The final product was stored as a colloidal dispersion at 4°C for characterization and adsorption experiments. For comparison, bulk MoS_2 powder was used directly in adsorption experiments without any additional treatment, representing the unmodified control material.

2.3. Adsorption experiments

All adsorption experiments were conducted under batch conditions in a temperature-controlled shaker (HZQ-F160, Shanghai Yiheng Scientific Instrument Co., Ltd., China) operated at 25 ± 1°C. For each test, 100 mL of metal ion solution with known concentrations was placed in 250 mL conical flasks, and the desired amount of adsorbent (either bulk MoS_2 or MoS_2 nanosheets) was added. The pH of the solution was adjusted prior to the experiments and maintained throughout.

Adsorption isotherm investigations were conducted by adjusting the initial concentrations of metal ions (Cd^{2+}, Cu^{2+}, and Pb^{2+}) within the range of 5 to 200 mg/L, with the adsorbent dosage maintained at a constant value of 0.5 g/L. The influence of pH on adsorption was examined over a pH range of 2 to 8. The effect of competing ions, including Na^{+}, K^{+}, Ca^{2+}, and Mg^{2+} at concentrations of 0.01 M, was also investigated to simulate the conditions of real AMD.

3. Results and discussion

3.1. Material characterization

The crystallographic structures of the synthesized materials were investigated using XRD (Figure 1a). The diffraction patterns, as shown in Figure 1a, confirm the presence of the characteristic hexagonal 2H-MoS_2 phase for both bulk and exfoliated samples [19]. For bulk MoS_2, sharp and intense diffraction peaks were observed at 2θ values of 14.4°, 32.7°, 39.5°, and 58.3°, corresponding to the (002), (100), (103), and (110) planes, respectively, in good agreement with JCPDS card no. 37-1492 [20]. After exfoliation, the XRD pattern of the MoS_2 nanosheets exhibited significant broadening and a noticeable decrease in peak intensity, particularly for the (002) plane. This broadening indicates a reduction in crystallite size along the c-axis and a decrease in the number of stacked layers [21]. Furthermore, a slight shift of the (002) peak to a lower 2θ angle was recorded, suggesting an increase in the interlayer spacing from 0.62 nm to approximately 0.72 nm. These observations confirm successful exfoliation and the formation of few-layer MoS_2 nanosheets.

The morphology of the materials was further examined using SEM and TEM analyses (Figures 1b–1e). The SEM image of bulk MoS_2 (Figure 1b) reveals a typical aggregated structure with thick, multilayered flakes tightly stacked together, forming large particle clusters with sizes ranging from 2 to 5 μm. Such structures inherently limit the accessibility of active sites, thereby reducing their efficiency in adsorption applications. In contrast, the SEM image of exfoliated MoS_2 nanosheets (Figure 1c) displays ultrathin, wrinkled sheets with highly dispersed morphology. TEM analysis further supports these observations. As shown in Figure 1d, the bulk MoS_2 exhibits dense, thick lamellar structures, whereas the exfoliated MoS_2 nanosheets (Figure 1e) exhibit transparent sheets with lateral dimensions of approximately 300–500 nm. High-resolution TEM revealed that the exfoliated nanosheets predominantly consist of 1–2 layers, with an interlayer spacing of approximately 0.72 nm, corroborating the XRD findings [22]. These morphological changes significantly enhance the material's surface area and expose a higher density of active adsorption sites, critical for effective heavy metal ion binding.

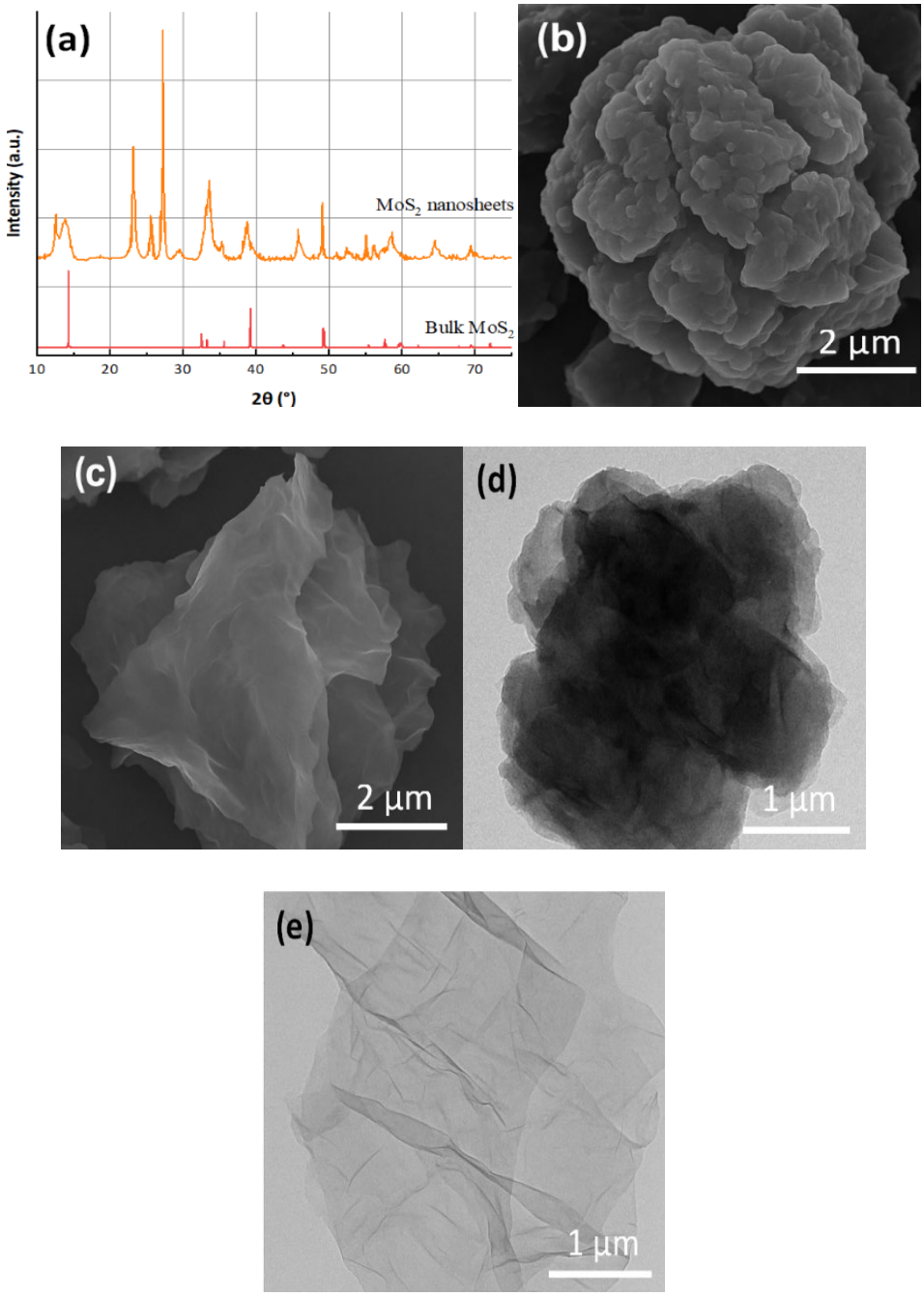

Fig. 1. (a) XRD patterns of bulk MoS_2 and exfoliated MoS_2 nanosheets. (b) SEM image of bulk MoS_2 showing aggregated multilayer structures. (c) SEM image of exfoliated MoS_2 nanosheets exhibiting thin, wrinkled layers. (d) TEM image of bulk MoS_2 confirming thick lamellar stacking. (e) TEM image of MoS_2 nanosheets showing transparent, few-layer structures with increased lateral dispersion.

The BET method was employed to analyze the specific surface areas and pore structures of the samples. The adsorption–desorption isotherms of both samples exhibit Type IV curves with H3 hysteresis loops, characteristic of mesoporous materials [23]. As outlined in Table 1, the BET surface area of bulk MoS_2 was found to be 5.6 m^2/g, accompanied by an average pore diameter of 12.4 nm

and an overall pore volume of 0.015 cm^3/g. After exfoliation, the surface area of MoS_2 nanosheets increased dramatically to 26.6 m^2/g, accompanied by a reduction in the average pore diameter to 8.7 nm and an increase in pore volume to 0.042 cm^3/g [24]. This significant enhancement in surface area and porosity provides more accessible active sites for adsorption, which is expected to contribute substantially to the improved heavy metal ion adsorption capacity observed in subsequent experiments.

Table 1. BET surface area, average pore diameter, and pore volume of bulk MoS_2 and MoS_2 nanosheets.

Sample	BET Surface Area (m^2/g)	Average Pore Diameter (nm)	Pore Volume (cm^3/g)
Bulk MoS_2	5.6	12.4	0.015
MoS_2 Nanosheets	26.6	8.7	0.042

The wide-scan XPS spectra (Figure 2a) confirmed the presence of Mo and S elements, with no detectable impurities [25]. Detailed high-resolution spectra of Mo 3d (Figure 2b) for MoS_2 show characteristic doublet peaks at binding energies of 229.4 eV (Mo $3d_{5/2}$) and 232.6 eV (Mo $3d_{3/2}$), corresponding to Mo^{4+} in the 2H-MoS_2 phase [26]. Similarly, the S 2p spectra (Figure 2c) display doublet peaks at 161.8 eV (S $2p_{3/2}$) and 163.0 eV (S $2p_{1/2}$), typical for sulfide ions (S^{2-}) in MoS_2 [27]. Additionally, the appearance of a weak peak at 168.5 eV indicates minor surface oxidation, likely due to the exfoliation process.

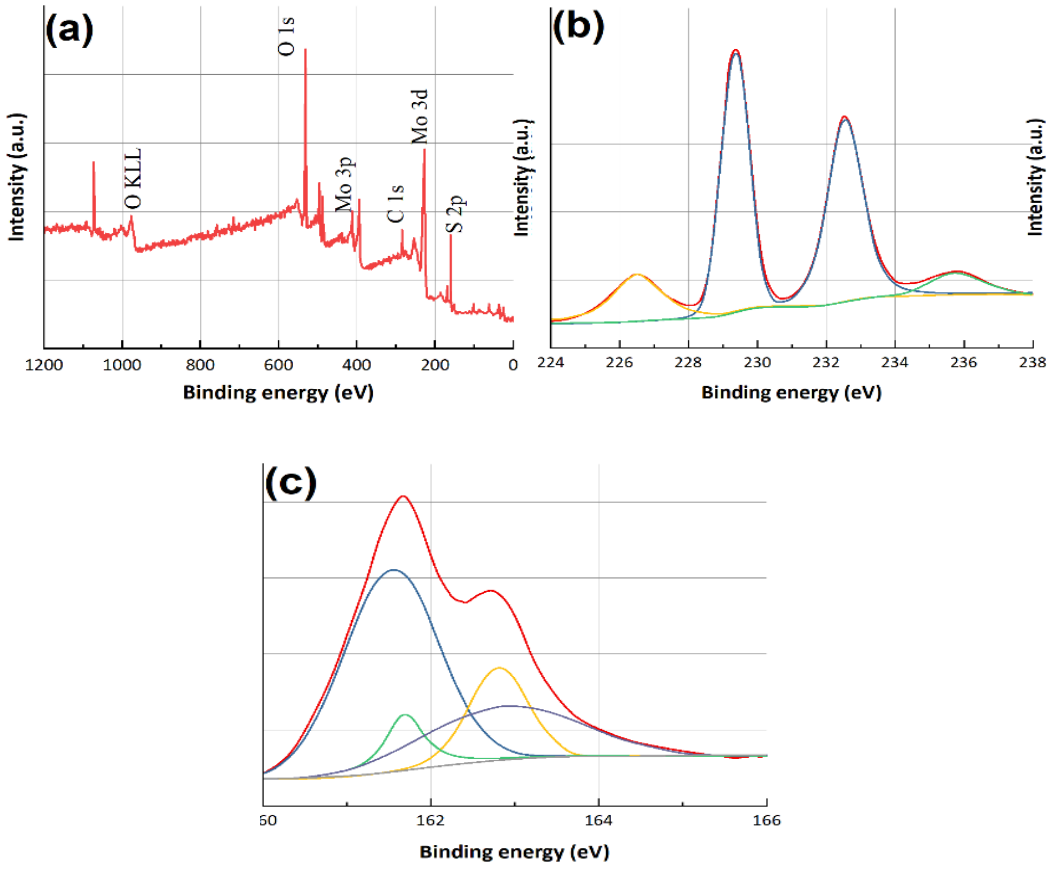

Fig. 2. (a) XPS wide-scan spectra of exfoliated MoS_2. (b) High-resolution Mo 3d spectra showing chemical state. (c) High-resolution S 2p spectrum indicating increased surface sulfur exposure post-exfoliation.

3.2. Adsorption performance evaluation

The adsorption equilibrium data for Cd^{2+}, Cu^{2+}, and Pb^{2+} ions onto both bulk MoS_2 and MoS_2 nanosheets (MoS_2 NS) were analyzed. The resulting isotherms are presented in Figures 3a–4c, and the calculated model parameters are summarized in Tables 2 and 3.

For all three metal ions, the Langmuir model provided a superior fit, as indicated by higher correlation coefficients (R^2 values ranging from 0.982 to 0.995 for MoS_2 NS) compared to the Freundlich model (R^2 values below 0.93). This suggests that the adsorption process is dominated by monolayer coverage of the adsorbate on a homogeneous surface with finite adsorption sites, particularly for MoS_2 NS. The maximum adsorption capacities (q_m) reveal a significant improvement in adsorption performance for MoS_2 NS compared to bulk MoS_2. For Pb^{2+} ions, MoS_2 NS exhibited the highest adsorption capacity of 200 mg/g, while the bulk counterpart showed a considerably lower value of 78 mg/g. Similarly, the maximum capacities for Cd^{2+} and Cu^{2+} were determined to be 185 mg/g and 170 mg/g for MoS_2 NS, respectively, compared to 65 mg/g and 58 mg/g for bulk MoS_2.

The enhancement in adsorption performance can be attributed to the larger specific surface area [28], increased porosity, and greater availability of reactive sulfur sites on the exfoliated nanosheets, as confirmed in the material characterization section [29]. These structural features facilitate efficient metal ion coordination, particularly through strong chemical interactions between heavy metals and sulfur atoms [30]. The Langmuir constant (K_l), which reflects the affinity of the adsorbent for the adsorbate, was also markedly higher for MoS_2 NS across all ions, indicating stronger binding interactions. The dimensionless separation factor (RL) calculated for the Langmuir model remained between 0 and 1 for all cases, confirming the favorability of the adsorption process [31].

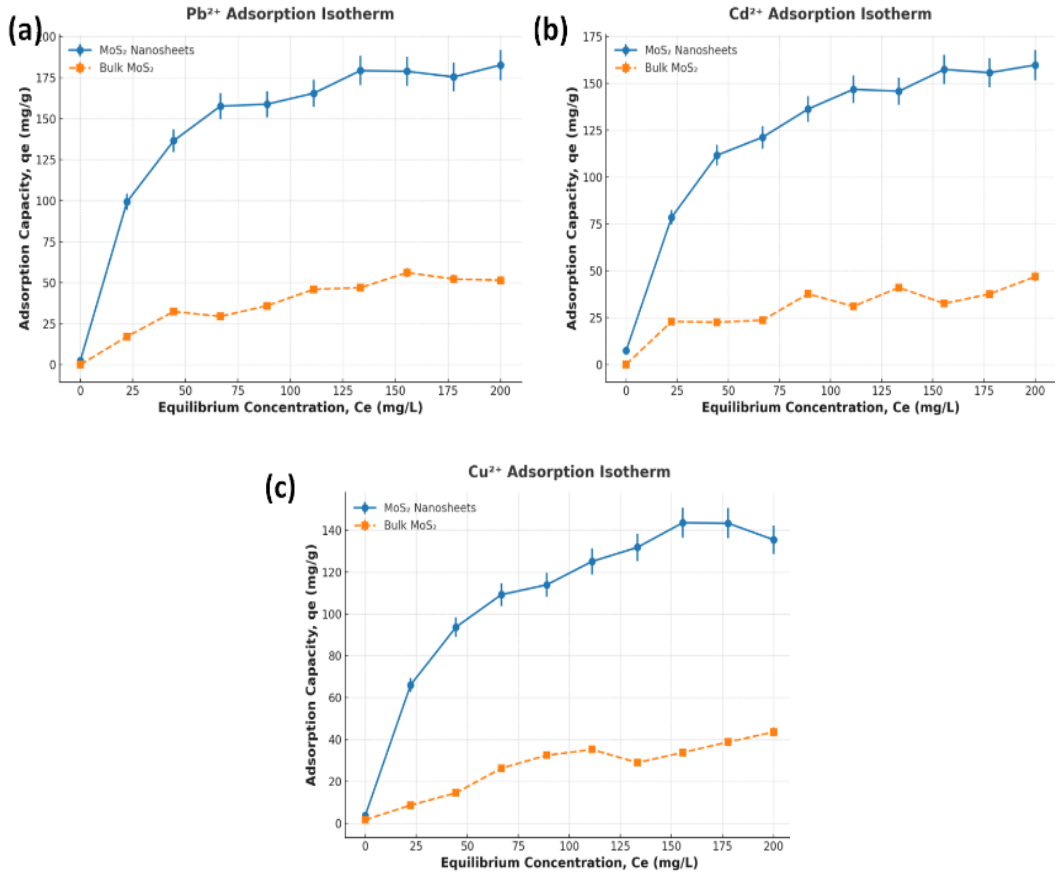

Fig. 3. Langmuir isotherm plot for (a) Cd^{2+}, (b) Cu^{2+} and (c) Pb^{2+} adsorption on bulk MoS_2 and MoS_2 NS.

Table 2. Langmuir isotherm parameters for heavy metal ion adsorption.

Adsorbent	Metal Ion	q_m (mg/g)	K_l (L/mg)	R^2
Bulk MoS_2	Cd^{2+}	65	0.012	0.928
MoS_2 Nanosheets	Cd^{2+}	185	0.034	0.991
Bulk MoS_2	Cu^{2+}	58	0.010	0.915
MoS_2 Nanosheets	Cu^{2+}	170	0.028	0.988
Bulk MoS_2	Pb^{2+}	78	0.015	0.936
MoS_2 Nanosheets	Pb^{2+}	200	0.045	0.995

Table 3. Freundlich isotherm parameters for heavy metal ion adsorption.

Adsorbent	Metal Ion	Kf (mg/g)	n	R^2
Bulk MoS_2	Cd^{2+}	14.3	1.62	0.885
MoS_2 Nanosheets	Cd^{2+}	49.6	2.45	0.923
Bulk MoS_2	Cu^{2+}	12.7	1.54	0.872
MoS_2 Nanosheets	Cu^{2+}	45.3	2.36	0.918
Bulk MoS_2	Pb^{2+}	16.5	1.68	0.893
MoS_2 Nanosheets	Pb^{2+}	54.1	2.60	0.929

The adsorption kinetics of Cd^{2+}, Cu^{2+}, and Pb^{2+} ions were investigated to assess the rate-controlling mechanisms [32]. The fitting results and kinetic parameters are presented in Figures 4a–5c and Table 4. For all metal ions, MoS_2 NS achieved rapid adsorption, with more than 90% of total uptake completed within the first 30 minutes [33]. Equilibrium was reached after approximately 60 minutes, highlighting the fast kinetics of MoS_2 NS, which is advantageous for practical water treatment applications. In contrast, bulk MoS_2 required significantly longer times to approach equilibrium, often exceeding 180 minutes. Model fitting results revealed that the pseudo-second-order kinetic model provided a much better correlation with the experimental data for both MoS_2 NS and bulk MoS_2 [34]. The calculated rate constants (k_2) for MoS_2 NS were significantly higher than those for bulk MoS_2, further confirming the superior adsorption kinetics of the nanosheets [35]. This behavior is attributed to the higher density of accessible active sites and improved diffusion pathways within the nanosheet structure, facilitating faster interaction between the adsorbent and metal ions [36].

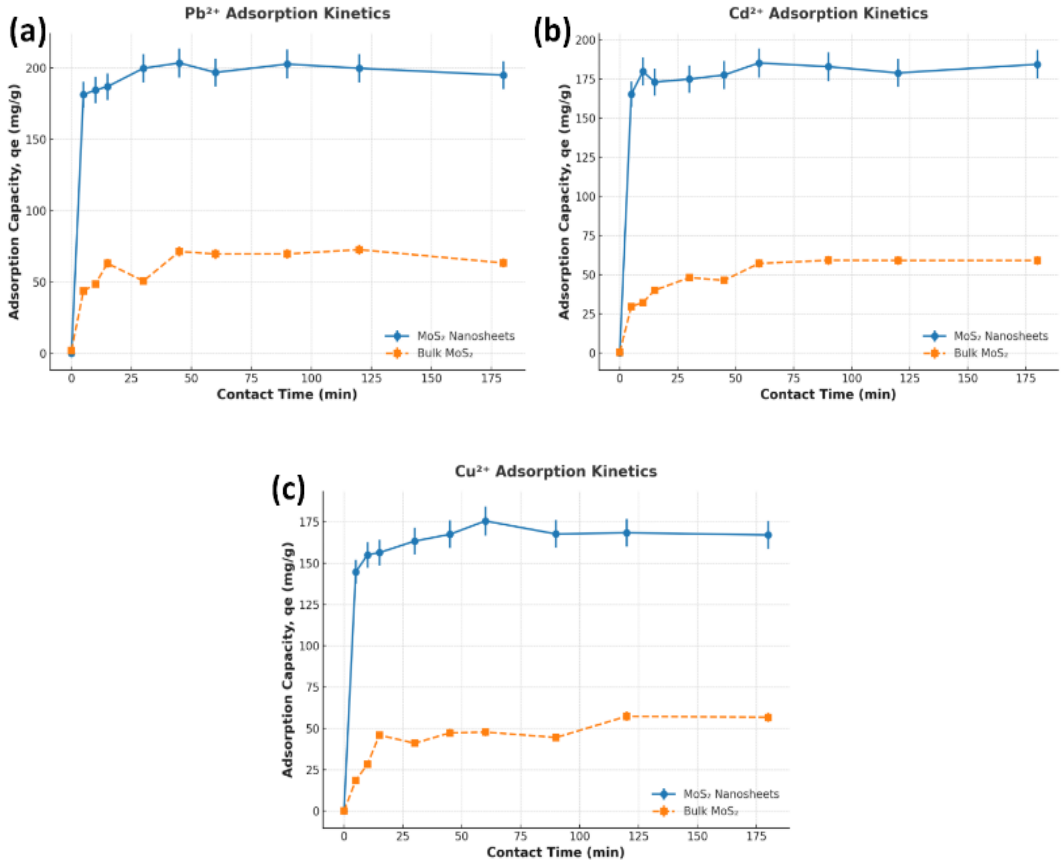

Fig. 4. Adsorption kinetics of (a) Cd^{2+}, (b) Cu^{2+} and (c) Pb^{2+} on bulk MoS_2 and MoS_2 NS fitted with the pseudo-second-order model.

Table 4. Pseudo-second-order kinetic parameters.

Adsorbent	**Metal Ion**	**k_2 (g/mg·min)**	**qe (mg/g)**	**R^2**
Bulk MoS_2	Cd^{2+}	0.0021	62.8	0.911
MoS_2 Nanosheets	Cd^{2+}	0.0095	182.3	0.987
Bulk MoS_2	Cu^{2+}	0.0018	55.9	0.899
MoS_2 Nanosheets	Cu^{2+}	0.0082	168.1	0.984
Bulk MoS_2	Pb^{2+}	0.0024	75.5	0.915
MoS_2 Nanosheets	Pb^{2+}	0.0111	198.7	0.992

3.3. Mechanistic insights

The FTIR spectra of MoS_2 nanosheets prior to adsorption exhibited characteristic peaks at 470 cm^{-1} and 620 cm^{-1}, corresponding to the Mo–S stretching vibrations in the 2H phase (Figure 5a) [19]. After adsorption of Pb^{2+}, Cd^{2+}, and Cu^{2+}, noticeable shifts and intensity reductions were observed in these peaks [37]. Additionally, a new weak band appeared around 700–720 cm^{-1}, which is attributed to the formation of metal-sulfur (M–S) bonds.

XPS analysis provided further confirmation of the chemical interactions between metal ions and MoS_2 nanosheets [38]. The high-resolution Mo 3d spectra (Figure 5b) showed slight shifts to lower binding energies after adsorption, suggesting increased electron density around Mo atoms due to the formation of M–S bonds. More significantly, the S 2p spectra (Figure 5c) displayed an additional peak at approximately 162.5 eV after metal ion adsorption, corresponding to the formation of M–S complexes. These observations confirm that sulfur atoms on the MoS_2 surface play a dominant role in the chemisorption process by forming stable complexes with heavy metal ions.

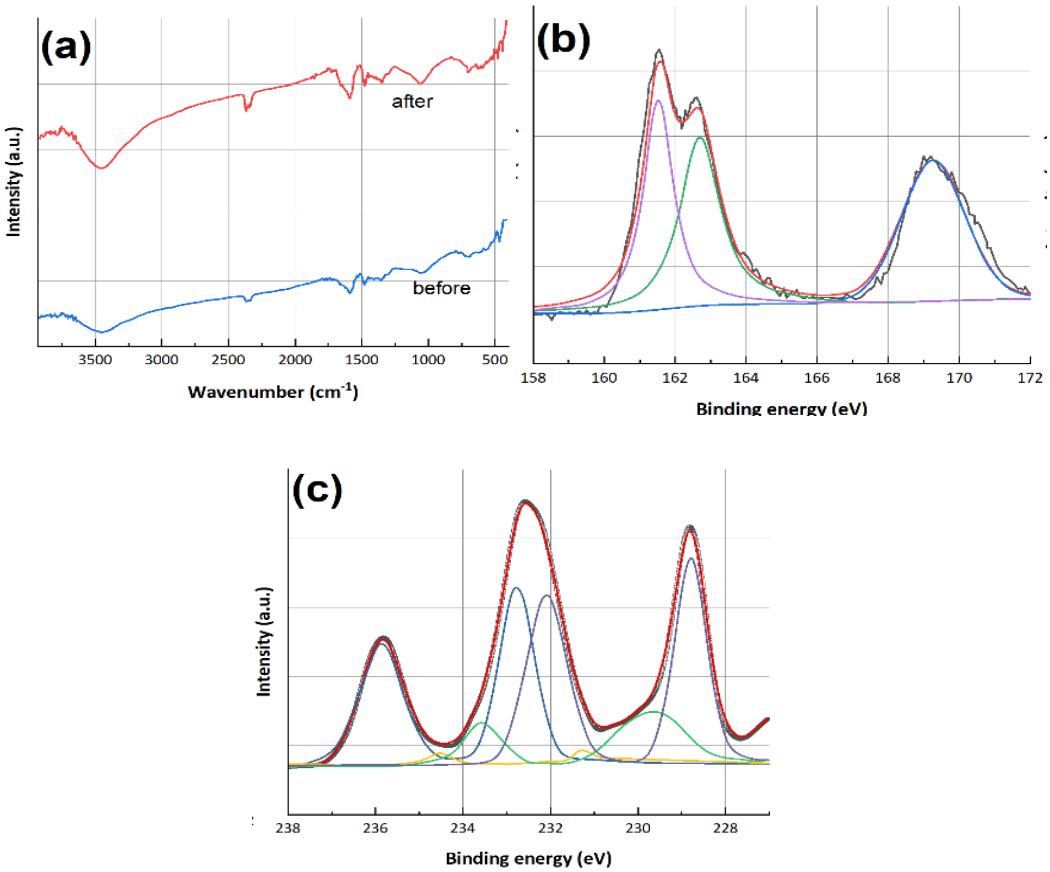

Fig. 5. (a) FTIR spectra of MoS_2 nanosheets before and after adsorption of Pb^{2+}, Cd^{2+}, and Cu^{2+}, indicating the formation of M–S bonds. (b) High-resolution XPS Mo 3d spectra before and after metal ion adsorption showing shifts in binding energies. (c) High-resolution XPS S 2p spectra revealing the emergence of M–S complexation peaks post-adsorption.

The pH of the solution plays a crucial role in modulating the surface charge of MoS_2 nanosheets and the speciation of metal ions, thus directly influencing the adsorption efficiency. To investigate this effect, adsorption experiments were conducted over a pH range of 2 to 8, and the results are illustrated in Figure 6. At highly acidic conditions (pH < 3), the adsorption capacities for all metal ions were significantly suppressed [39]. This reduction is attributed to the competitive adsorption of protons (H^+) on the sulfur active sites, which blocks the binding of metal ions. Additionally, under low pH conditions, the surface of MoS_2 nanosheets remains positively charged,

as confirmed by Zeta potential measurements (Figure 6a inset).

As the pH increased from 3 to 6, a substantial enhancement in adsorption capacity was observed [40]. The optimal adsorption performance for all metal ions was achieved in the pH range of 5–6 [41]. At this pH, the Zeta potential of MoS_2 nanosheets shifts from positive to slightly negative values, promoting electrostatic attraction between the negatively charged adsorbent surface and cationic metal species. Simultaneously, deprotonation of surface functional groups enhances the availability of sulfur active sites for complexation [42]. Beyond pH 6, a slight decline in adsorption was noted, particularly for Pb^{2+} [43]. This phenomenon is attributed to the potential precipitation of metal hydroxides, such as $Pb(OH)_2$ and $Cd(OH)_2$, which reduces the availability of free metal ions in solution for adsorption [44]. Therefore, the optimal pH range of 5–6 ensures maximum adsorption through a synergistic effect of electrostatic attraction and chemical complexation while minimizing the precipitation of metal ions.

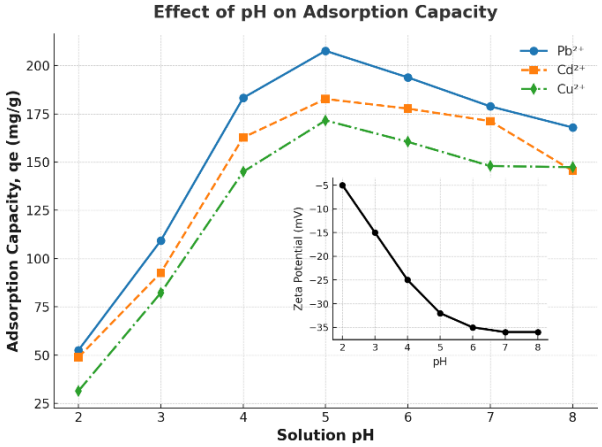

Fig. 6. Effect of solution pH on the adsorption capacities of Pb^{2+}, Cd^{2+}, and Cu^{2+} by MoS_2 nanosheets. The inset shows the corresponding Zeta potential variations with pH.

To further confirm the successful adsorption of heavy metal ions onto the MoS_2 nanosheets, SEM coupled with EDS elemental mapping was conducted. Figure 9 presents the morphological features and elemental distribution of Cu, Pb, and Cd on the surface of MoS_2 nanosheets after the adsorption process. The SEM image (Figure 7a) clearly shows a well-defined, rough, and layered surface structure of the MoS_2 nanosheets. The nanosheets exhibit a wrinkled and loosely stacked morphology, providing numerous adsorption sites for metal ions.

The corresponding EDS elemental mapping images (Figures 7b–d) distinctly reveal the spatial distribution of the adsorbed metal ions. The mapping of Cu (Figure 8b) illustrates a homogeneous distribution of Cu across the entire surface of the nanosheets, indicating uniform adsorption. Similarly, the Pb mapping (Figure 7c) shows a strong and localized presence of Pb ions, further confirming the preferential adsorption of Pb^{2+} due to its higher affinity toward sulfur functional groups. The Cd mapping (Figure 7d) also demonstrates a widespread distribution of Cd^{2+} ions, supporting the high adsorption capacity observed in the batch experiments. The clear and distinct elemental distributions in the EDS maps confirm that the adsorption process involves strong chemical interactions between the metal ions and the sulfur active sites of MoS_2 nanosheets.

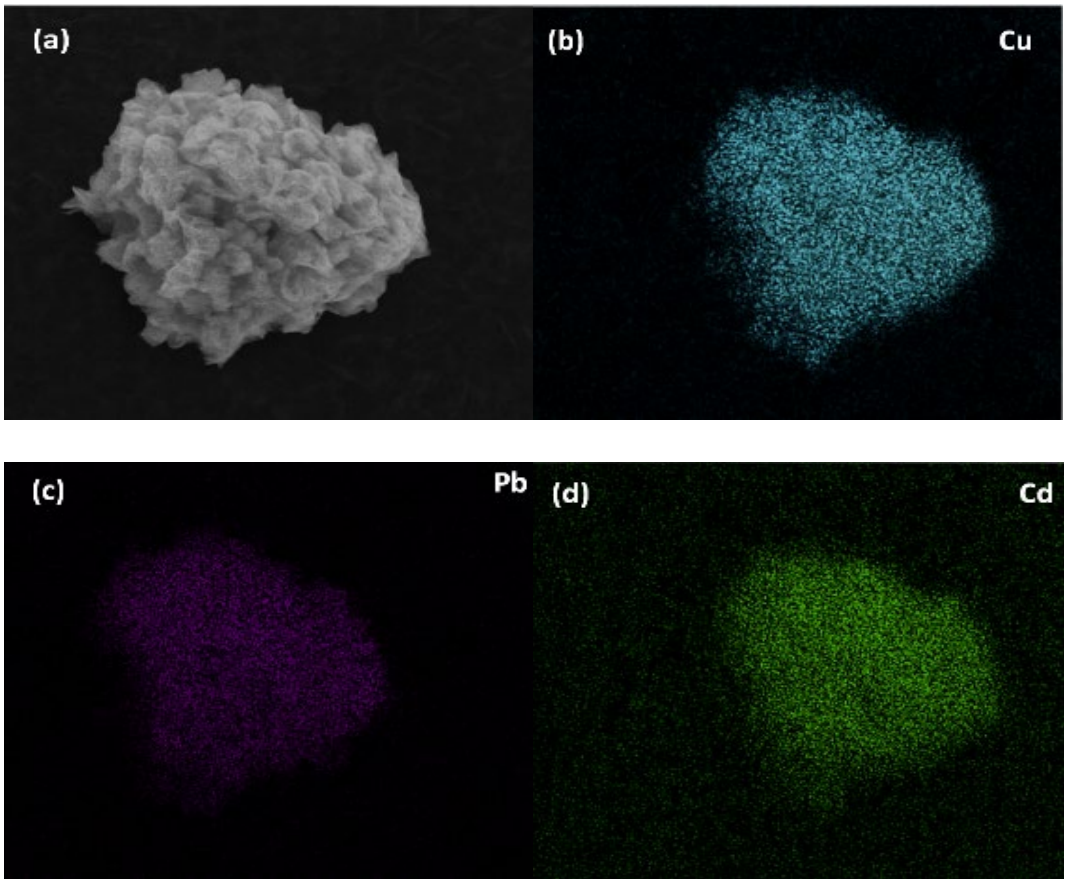

Fig. 7. (a) SEM morphological image of MoS_2 nanosheets after adsorption of heavy metal ions. (b–d) EDS elemental mapping images of Cu, Pb, and Cd, respectively.

3.4. Proposed adsorption mechanism

According to the experimental observations and analytical outcomes, a thorough adsorption mechanism is put forward for the elimination of heavy metal ions by MoS_2 nanosheets (depicted in Figure 8). The mechanism involves three primary pathways:

1. Physical Hole-Filling Effect: The exfoliation of bulk MoS_2 into ultrathin nanosheets significantly enhances its specific surface area and pore volume, as evidenced by BET analysis. The mesoporous structure facilitates the physical entrapment of metal ions within the nanoscale pores, contributing to initial adsorption through van der Waals interactions. Although this effect plays a secondary role compared to chemisorption, it accelerates the mass transfer and diffusion of metal ions towards active adsorption sites.

2. Electrostatic Attraction: Under near-neutral pH conditions, the MoS_2 nanosheet surfaces acquire a negative charge, as confirmed by Zeta potential measurements. This charge development enhances electrostatic interactions between the negatively charged adsorbent and positively charged metal ions in solution. While this mechanism promotes the rapid initial uptake of metal ions, it is less dominant at lower pH values due to surface protonation.

3. Chemical Complexation (M–S Bond Formation): The most significant contribution to adsorption arises from the formation of stable metal-sulfur (M–S) complexes. FTIR and XPS analyses confirm the strong coordination between metal ions and the exposed sulfur atoms on the

nanosheet surfaces. This chemisorption process involves electron sharing between the soft Lewis base (S^{2-}) and the soft acid metal cations (Pb^{2+}, Cd^{2+}, and Cu^{2+}), leading to the formation of highly stable complexes. This explains the superior adsorption capacities and fast kinetics observed for MoS_2 nanosheets.

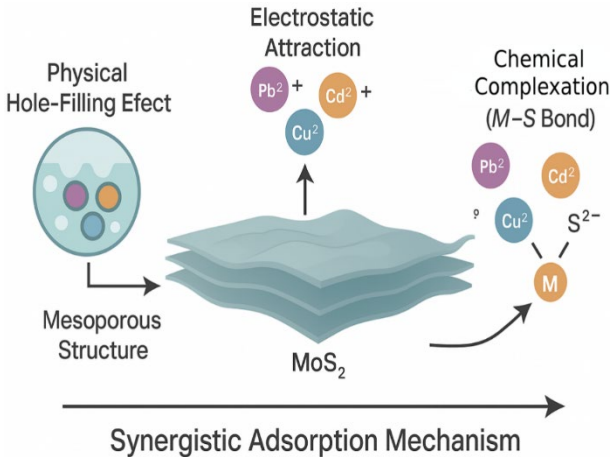

Fig. 8. Proposed schematic of the adsorption mechanisms for heavy metal ions on MoS_2 nanosheets, illustrating physical hole-filling, electrostatic attraction, and chemical complexation pathways.

4. Conclusion

In this study, two-dimensional MoS_2 nanosheets were successfully synthesized via a liquid-phase exfoliation technique and demonstrated remarkable efficiency in removing heavy metal ions from AMD. Compared to bulk MoS_2, the exfoliated nanosheets exhibited significantly enhanced adsorption capacities, achieving maximum values of 200 mg/g for Pb^{2+}, 185 mg/g for Cd^{2+}, and 170 mg/g for Cu^{2+}. This superior performance is attributed to their increased specific surface area, expanded interlayer spacing, and higher availability of reactive sulfur sites, as confirmed through comprehensive material characterizations including XRD, SEM/TEM, BET, and XPS analyses. Adsorption isotherm studies revealed that the process followed the Langmuir model, indicating monolayer adsorption dominated by chemisorption mechanisms. Mechanistic investigations using FTIR and XPS demonstrated that the primary adsorption pathway involved the formation of strong metal–sulfur (M–S) bonds, supported by additional contributions from electrostatic interactions and physical hole-filling effects. The adsorption process was highly pH-dependent, with optimal removal observed at near-neutral pH conditions due to the favorable surface charge of the MoS_2 nanosheets. Overall, this research offers a thorough comprehension of the structural benefits and adsorption mechanisms of MoS_2 nanosheets. It provides valuable perspectives for the creation of advanced, high - efficiency, and eco - friendly adsorbents, which can be used for the treatment of wastewater contaminated by heavy metals.

Acknowledgements

This work was supported by Shanxi Provincial Department of Science and Technology Project: "Research on the mechanism of non-forced roof cutting and self-forming roadway along goaf in close range coal seam goaf" (202103021224336) and Research on Key Technologies for Grouting Reinforcement of Surrounding Rock of Fault Fracture Zone and Small Coal Pillars of the Wangjialing Mining (No.:2024HX-19).

References

[1] S. Li, L. Yu, W. Jiang, H. Yu, X. Wang, International Journal of Environmental Research and Public Health 19, 5673 (2022); https://doi.org/10.3390/ijerph19095673

[2] M. Hermassi, M. Granados, C. Valderrama, C. Ayora, J. L. Cortina, Science of the Total Environment 810, 152258 (2022); https://doi.org/10.1016/j.scitotenv.2021.152258

[3] K. K. Brar, S. Etteieb, S. Magdouli, L. Calugaru, S. K. Brar, Journal of Environmental Management 308, 114507 (2022); https://doi.org/10.1016/j.jenvman.2022.114507

[4] J. Briffa, E. Sinagra, R. Blundell, Heliyon 6, e04691 (2020); https://doi.org/10.1016/j.heliyon.2020.e04691

[5] N. B. Saidon, R. Szabó, P. Budai, J. Lehel, Environmental Pollution 340, 122815 (2024); https://doi.org/10.1016/j.envpol.2023.122815

[6] B. Nguegang, V. Masindi, T. A. M. Msagati, M. Tekere, Minerals 11, 477 (2021); https://doi.org/10.3390/min11050477

[7] C. O. A. Turingan, G. B. Singson, B. T. Melchor, R. D. Alorro, A. B. Beltran, A. H. Orbecido, Minerals 10, 845 (2020); https://doi.org/10.3390/min10100845

[8] E. Anifah, I. K. Ariani, J. T. P. Tindaon, Basransyah, Sustinere: Journal of Environment and Sustainability 8, 44 (2024); https://doi.org/10.22515/sustinere.jes.v8i1.366

[9] M. Paradise, E. Nursanto, N. Nurkhamim, S. R. Haq, ASEAN Engineering Journal 12, 75 (2022); https://doi.org/10.11113/aej.v12.16982

[10] K. Gupta, P. Joshi, R. Gusain, O. P. Khatri, Coordination Chemistry Reviews 445, 214100 (2021); https://doi.org/10.1016/j.ccr.2021.214100

[11] P. Liu, M. Huo, J. Shi, CCS Chemistry 3, 2445 (2021); https://doi.org/10.31635/ccschem.020.202000519

[12] X. Ji, L. Ge, C. Liu, Z. Tang, Y. Xiao, W. Chen, Z. Lei, W. Gao, S. Blake, D. De, B. Shi, X. Zeng, N. Kong, X. Zhang, W. Tao, Nature Communications 12, 1124 (2021).

[13] W. Wang, X. Zhang, Y. Zhang, X. Chen, J. Ye, J. Chen, Z. Lyu, X. Chen, Q. Kuang, S. Xie, Z. Xie, Nano Letters 20, 5458 (2020); https://doi.org/10.1021/acs.nanolett.0c01908

[14] H. Ganesha, S. Veeresh, Y. S. Nagaraju, M. Vandana, M. Basappa, H. Vijeth, H. Devendrappa, Nanoscale Advances 4, 521 (2022); https://doi.org/10.1039/D1NA00664A

[15] S. Sharifi, K. Rahimi, A. Yazdani, Scientific Reports 11, 8378 (2021); https://doi.org/10.1038/s41598-021-87823-6

[16] X. Zheng, Y. Liu, Y. Yang, Y. Song, P. Deng, J. Li, W. Liu, Y. Shen, X. Tian, Renewables 1,

39 (2023); https://doi.org/10.31635/renewables.022.202200001

[17] Q. Han, H. Cao, Y. Sun, G. Wang, S. Poon, M. Wang, B. Liu, Y. Wang, Z. Wang, B. Mi, Physical Chemistry Chemical Physics 24, 13305 (2022); https://doi.org/10.1039/D2CP00705C

[18] W. Tian, L. Wu, R. Huang, A. Wang, Y. Lu, N. Tang, L. Gao, AIP Advances 14, 25017 (2024); https://doi.org/10.1063/5.0187789

[19] Z. Zhou, L. Zhao, Y. Liu, D. Li, Q. Xia, J. Wang, Z. Zhang, X. Han, Y. Long, Y. Zhang, Y. Li, S. Chou, Renewables 1, 100 (2023); https://doi.org/10.31635/renewables.022.202200004

[20] S. Imai, T. Tatsumi, S. Tomiya, K. Kakushima, H. Wakabayashi, ECS Meeting Abstracts MA2024-2, 1791 (2024); https://doi.org/10.1149/MA2024-02201791mtgabs

[21] M. Kigozi, R. K. Koech, O. Kingsley, I. Ojeaga, E. Tebandeke, G. N. Kasozi, A. P. Onwualu, Results in Materials 7, 100113 (2020); https://doi.org/10.1016/j.rinma.2020.100113

[22] K. Ma, Y. Liu, H. Jiang, Y. Hu, R. Si, H. Liu, C. Li, CCS Chemistry 3, 1472 (2021); https://doi.org/10.31635/ccschem.020.202000323

[23] G. Ji, Y. Wang, W. Ye, M. Chen, F. Zhang, Y. Zhao, S. Tong, B. Han, Z. Liu, CCS Chemistry 5, 1854 (2023); https://doi.org/10.31635/ccschem.022.202202187

[24] X. Yin, A. Teng, Z. Zeng, H. Meng, W. Wu, SSRN Electronic Journal (2022).

[25] B. Pandit, B. R. Sankapal, ACS Applied Nano Materials 5, 3007 (2022); https://doi.org/10.1021/acsanm.2c00374

[26] Z. Xue, C. Wang, Y. Tong, M. Yan, J. Zhang, X. Han, X. Hong, Y. Li, Y. Wu, CCS Chemistry 4, 3842 (2022); https://doi.org/10.31635/ccschem.022.202101628

[27] Z. Liu, K. Nie, Y. Yuan, B. Li, P. Liu, S. Chong, Y. Du, W. Huang, CCS Chemistry 4, 3391 (2022); https://doi.org/10.31635/ccschem.021.202101598

[28] J. Zhao, Z. Zhao, K. Li, R. Zhao, H. Zhao, Microporous and Mesoporous Materials 377, 113215 (2024); https://doi.org/10.1016/j.micromeso.2024.113215

[29] L. Liu, Y. Gong, Y. Tong, H. Tian, X. Wang, Y. Hu, S. Huang, W. Huang, S. Sharma, J. Cui, Y. Jin, W. Gong, W. Zhang, CCS Chemistry 6, 1255 (2024); https://doi.org/10.31635/ccschem.024.202403938

[30] X. Zhou, Y. Liu, C. Jin, G. Wu, G. Liu, Z. Kong, RSC Advances 12, 1130 (2022); https://doi.org/10.1039/D1RA06774E

[31] E. E. Abdel-Hady, H. F. M. Mohamed, S. H. M. Hafez, A. M. M. Fahmy, A. Magdy, A. S. Mohamed, E. O. Ali, H. R. Abdelhamed, O. M. Mahmoud, Scientific Reports 13, 6435 (2023); https://doi.org/10.1038/s41598-023-33142-x

[32] J. Di, Z. Ruan, S. Zhang, Y. Dong, S. Fu, H. Li, G. Jiang, Scientific Reports 12, 1394 (2022).

[33] G. Nie, R. Ma, X. Wang, W. Wang, Q. Zhang, T. Jiao, Cell Reports Physical Science 5, 101756 (2024); https://doi.org/10.1016/j.xcrp.2023.101756

[34] H. Ashrafi, F. Rahnama, M. Akhond, G. Absalan, Inorganic Chemistry 61, 1118 (2022); https://doi.org/10.1021/acs.inorgchem.1c03290

[35] J. Hu, Y. Lu, X.-L. Liu, C. Janiak, W. Geng, S.-M. Wu, X.-F. Zhao, L.-Y. Wang, G. Tian, Y. Zhang, B.-L. Su, X.-Y. Yang, CCS Chemistry 2, 1573 (2020);

https://doi.org/10.31635/ccschem.020.202000305

[36] Y. Li, X. Zhang, Z. Zheng, CCS Chemistry 4, 31 (2022); https://doi.org/10.31635/ccschem.021.202101194

[37] H. Wu, T. Xia, F. Qi, S. Mei, Y. Xia, J.-F. Xu, X. Zhang, CCS Chemistry 5, 823 (2023); https://doi.org/10.31635/ccschem.022.202202410

[38] M. Vizza, W. Giurlani, L. Cerri, N. Calisi, A. A. Leonardi, M. J. L. Faro, A. Irrera, E. Berretti, J. V. Perales-Rondón, A. Colina, E. Bujedo Saiz, M. Innocenti, Molecules 27, 5416 (2022); https://doi.org/10.3390/molecules27175416

[39] W.-S. Chen, Y.-C. Chen, C.-H. Lee, Processes 10, 150 (2022); https://doi.org/10.3390/pr10010150

[40] W. Nie, J. Liu, X. Bai, Z. Xing, Y. Gao, Polymers 14, 203 (2022); https://doi.org/10.3390/polym14010203

[41] B. A. Ezeonuegbu, D. A. Machido, C. M. Z. Whong, W. S. Japhet, A. Alexiou, S. T. Elazab, N. Qusty, C. A. Yaro, G. E.-S. Batiha, Biotechnology Reports 30, e00614 (2021); https://doi.org/10.1016/j.btre.2021.e00614

[42] D. I. Nazarov, J. Labella, A. V. Kuzmin, M. A. Faraonov, E. N. Ivanov, S. S. Khasanov, T. Torres, M. K. Islyaikin, D. V. Konarev, CCS Chemistry 6, 1731 (2024); https://doi.org/10.31635/ccschem.024.202303824

[43] F. B. Kheyrabadi, E. N. Zare, Scientific Reports 12, 4632 (2022); https://doi.org/10.1038/s41598-022-08668-1

[44] P. Tangviroon, K. Noto, T. Igarashi, T. Kawashima, M. Ito, T. Sato, W. Mufalo, M. Chirwa, I. Nyambe, H. Nakata, S. Nakayama, M. Ishizuka, Minerals 10, 763 (2020); https://doi.org/10.3390/min10090763